Diffraction tomography for biochemical imaging with diffuse-photon density waves

X. D. Li, T. Durduran, and A. G. Yodh

Department of Physics and Astronomy, University of Pennsylvania, Philadelphia, Pennsylvania 19104

B. Chance

Department of Biochemistry and Biophysics, University of Pennsylvania, Philadelphia, Pennsylvania 19104

D. N. Pattanayak

GE Corporate Research and Development, Schenectady, New York 12301

Received November 5, 1996

The spatial structure of optically heterogeneous turbid media is probed with diffusive light. Projection images are obtained experimentally by deconvolution of the scattered diffuse-photon density waves on a planar boundary by use of a fast Fourier transform. The method is very fast, permitting object localization and characterization in ~1000 volume-element samples on subsecond computational time scales. The optical properties of slice-shape inhomogeneities are accurately determined. © 1997 Optical Society of America

Recently the application of near-IR diffusing light for biomedical diagnosis and imaging has gained favor because of its noninvasive nature, economy, and novel contrast relative to other diagnostics.[1–3] To this end a variety of techniques for imaging with diffuse light have been explored.[4,5] Most methods use direct matrix inversion (e.g., singular-value decomposition) or iterative techniques (e.g., algebraic reconstruction–simultaneous iterative reconstruction technique,[6] conjugate gradient descent) for image reconstruction.

Here we introduce a new near-field, diffusive-wave-imaging methodology, using techniques similar to those of conventional diffraction tomography.[7] The near-field diffraction tomography method has attracted the attention of a few researchers in the photon-migration field.[8] In this Letter present a rigorous account of the theory and provide the first experimental images of absorbing and scattering objects in turbid media obtained by this approach. The method differs from least-squares techniques[6] in that it is fast and noniterative. In addition to providing information about the position and shape of a hidden object or objects, *projection* images can be used to deduce the optical properties of heterogeneities without the need for complex reconstruction procedures such as matrix inversion when the heterogeneities are thin and information on their depth is available.

We adopt the frequency-domain picture for our discussion. An intensity sinusoidally modulated light source coupled into a highly scattering medium such as tissue produces a diffuse-photon density wave (DDPW) that propagates outward from the source.[9] The amplitude and phase of this DPDW depend on the absorption and the scattering coefficients within the turbid medium.

In uniform turbid media the DPDW from a point source at $\mathbf{r_s}$ detected at position $\mathbf{r_d}$ has the form $U_0(\mathbf{r_d}, \mathbf{r_s}, \omega) = M_0 \exp(ik_0|\mathbf{r} - \mathbf{r_s}|)/(4\pi D_0|\mathbf{r} - \mathbf{r_s}|)$. Here ω is the angular source-modulation frequency, M_0 is the ac amplitude of the source, $D_0 = v/(3\mu_{so}')$ is the diffusion coefficient (v is the speed of light in the medium), $k_0 = [(-\mu_{ao}v + i\omega)/D_0]^{1/2}$ is the DPDW wave number, and μ_{ao} and μ_{so}' are, respectively, the homogeneous absorption and the reduced scattering coefficients of the medium. In heterogeneous media, the total DPDW, $U_t(\mathbf{r_d}, \mathbf{r_s}, \omega)$, is a superposition of incident $[U_0(\mathbf{r_d}, \mathbf{r_s}, \omega)]$ and scattered $[U_1(\mathbf{r_d}, \mathbf{r_s}, \omega)]$ DPDW's. To the first order in the variation of optical absorption and reduced scattering coefficients, the scattered wave is

$$U_1(\mathbf{r_d}, \mathbf{r_s}, \omega) = \int_V T[U_0(\mathbf{r}, \mathbf{r_s}, \omega)] G(|\mathbf{r_d} - \mathbf{r}|) \mathrm{d}^3 r . \quad (1)$$

Here $G(|\mathbf{r_d} - \mathbf{r}|)$ is the Green's function for the DPDW in the homogeneous medium. We call $T[\mathbf{r}, U_0(\mathbf{r}, \mathbf{r_s}, \omega)]$ the inhomogeneity function. $T_{abs}[\mathbf{r}, U_0(\mathbf{r}, \mathbf{r_s}, \omega)] = (\delta\mu_a(\mathbf{r})v/D_0)U_0(\mathbf{r}, \mathbf{r_s}, \omega)$ for absorbing objects, and $T_{scatt}[\mathbf{r}, U_0(\mathbf{r}, \mathbf{r_s}, \omega)] = [\delta\mu_s'(\mathbf{r})3Doko^2/v) - \nabla \ln(\delta\mu_s' + \mu_{so}')] \cdot \nabla U_0(\mathbf{r}, \mathbf{r_s}, \omega)$ for scattering objects. The integral is over the sample volume V.

We consider a parallel-plane geometry [Fig. 1(a)] that is potentially applicable to the compressed-breast configuration. For this case, a natural basis set for the Green's function in Eq. (1) is the simple Weyl expansion form in terms of spatial frequencies p, q, m[10]:

$$G(|\mathbf{r_d} - \mathbf{r}|) = \frac{i}{8\pi^2} \int \int_{-\infty}^{\infty} \frac{\mathrm{d}p\mathrm{d}q}{m} \exp[ip(x_d - x) + iq(y_d - y) + im(z_d - z)], \quad (2)$$

where we assume that $z_d > z$ without losing generality; $m = (k_0^2 - p^2 - q^2)^{1/2}$ with $\mathrm{Im}(m) > 0$. Using Eq. (2) and taking the two-dimensional (2D) spatial Fourier transform of both sides of Eq. (1) [with respect to transverse (x, y) coordinates], we obtain

$$\tilde{U}_1(p, q, z_d, \mathbf{r_s}, \omega) = \frac{i}{2m} \int_{z_s}^{z_d} \tilde{T}(p, q, z, \mathbf{r_s}, \omega) \times \exp[im(z_d - z)]\mathrm{d}z . \quad (3)$$

The left side of Eq. (3) is the 2D Fourier transform of

0146-9592/97/080573-03$10.00/0

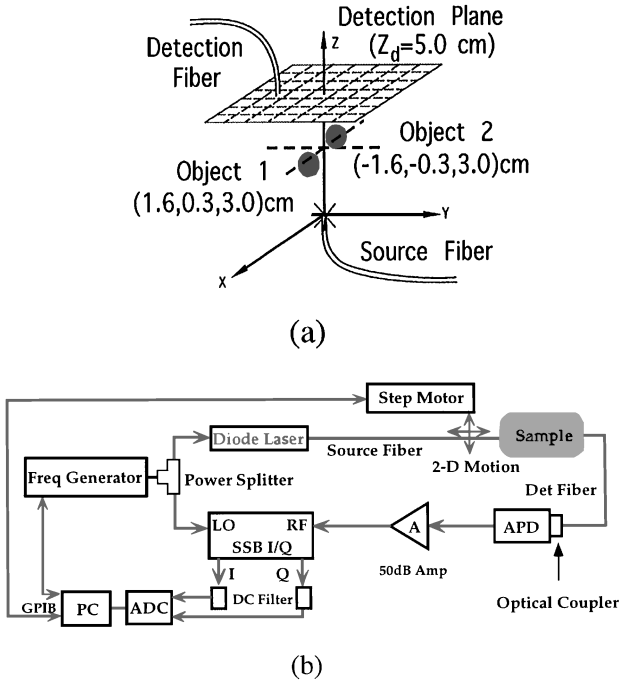

Fig. 1. (a) Experimental geometry: The source is fixed at the origin, and the detector scans in a planar geometry at $z = z_d = 5.0$ cm over a 9.3 cm $\times$ 9.3 cm region. (b) Setup: APD, avalanche photodiode; A, amplifier; SSB I/Q, single-sideband in-phase/quadrature-phase demodulator; LO, local port; RF, radiofrequency port; ADC, analog–digital converter; GPIB, general purpose interface bus.

the scattered DPDW measured on the detection plane $z = z_d$. This integral equation is approximated by

$$\sum_{j=1}^{N} \tilde{T}(p, q, z_j, \mathbf{r_s}, \omega)\exp(-mz_j) = \frac{2m}{i\delta z}\exp(-imz_d)\tilde{U}_1(p, q, z_d, \mathbf{r_s}, \omega), \quad (4)$$

where δz is the discretized step size and N is the total number of slices in the z direction.

For the *projection* image, we replace z_j on the left side of Eq. (4) with the estimated slice position of the object. We drop the sum over all other z_j's and then perform a 2D inverse Fourier transform of $\tilde{T}$ to obtain the projection image. When the object thickness is of the order of several transport mean free paths $[1/(\mu_a + \mu_s')]$, we can deduce accurately the optical properties of the object or objects. For thicker objects (i.e., >5 mm), the average over the size of the object weighted by the sum of exponential phase factors reduces the accuracy of the optical properties. However, position information is accurate, and the relative optical properties of multiple objects are also very accurate.

To demonstrate the feasibility of this algorithm, we performed amplitude and phase measurements in a parallel-plane geometry [Fig. 1(a)]. The experimental setup is shown in Fig. 1(b). The system consists of a rf-modulated (100-MHz), low-power (~3-mW) diode laser operating at 786 nm. The source light is fiber guided into a large fish tank of 50L 0.75% Intralipid ($\mu_a = 0.02$ cm^{-1}, $\mu_s' = 8.0$ cm^{-1}), enabling us to use infinite medium boundary conditions. A detection fiber couples the detected diffusive wave to a fast avalanche photodiode. A single-sideband demodulator is used to find the homodyne of the signal and the reference wave at 100 MHz. The dynamic range of our current setup is ~2500. The source and detection fiber optics are moved by automated stepper motors. The system is very stable for ~3 h.

The experimental geometry is shown in Fig. 1(a). The source position was fixed and taken to be the origin of our coordinate system. As shown in Fig. 1(a), we "made" the detection plane by scanning a single detection fiber over a square region from (−4.65, −4.65, 5.0) cm to (4.65, 4.65, 5.0) cm in a plane at $z_d = 5.0$ cm in steps of size $\Delta x = \Delta y = 0.3$ cm. The amplitude and phase of the DPDW were recorded at each position for a total of 1024 points. We directly measured the amplitude and phase in the homogeneous medium to obtain $U_0(\mathbf{r_d}, \mathbf{r_s}, \omega)$.

Two absorbing slices, each 1.5 cm $\times$ 1.5 cm $\times$ 0.4 cm were then submerged in the turbid medium (0.75% Intralipid). The slices were made of resin plus TiO_2 and absorbing dye. Slice 1 with $\mu_{a1} = 0.20$ cm^{-1} was placed at position (−1.6, −0.3, 3.0) cm, and slice 2 with $\mu_{a2} = 0.10$ cm^{-1} was placed at (1.6, 0.3, 3.0) cm. The scattering coefficients of these two slices are the same as that of the background, i.e., 8.0 cm^{-1}. We obtained the scattered wave $U_1(\mathbf{r_d}, \mathbf{r_s}, \omega)$ by subtracting the homogeneous background DPDW $U_0(\mathbf{r_d}, \mathbf{r_s}, \omega)$ from the measured signal $U_t(\mathbf{r_d}, \mathbf{r_s}, \omega)$. The 2D Fourier transform $U_1(\mathbf{r_d}, \mathbf{r_s}, \omega)$ leads to the inhomogeneity function $T(p, q, z_j, \mathbf{r_s}, \omega)$ in Eq. (4). We use *a priori* information about the object position(s) in the z direction to select a single image slice, e.g., a slice at $z = z_{\text{obj}}$, where the inhomogeneity function is $T(p, q, z_{\text{obj}}, \mathbf{r_s}, \omega)$. The 2D inverse Fourier transform of $T(p, q, z_{\text{obj}}, \mathbf{r_s}, \omega)$ gives an accurate spatial map of the absorption variations $\delta\mu_a(x, y, z_{\text{obj}})$.

The reconstructed images from the experimental data are shown in Fig. 2. The two objects are well resolved (with a peak–trough of >2). The reconstructed x–y positions of these two slices are approximately (−1.80, −0.25) cm and (1.85, 0.25) cm, close to their true x–y positions of (−1.6, −0.3) cm and (1.6, 0.3) cm. Inaccuracies in the position measurements might account for the discrepancy. Images shown in Figs. 2(b) and 2(d) are unprocessed. The reconstructed absorption coefficients are well above the background-noise level and close up to the true values [e.g., $\mu_{a1}^{\text{rec}} \approx (0.22 \pm 0.03)$ cm^{-1} and $\mu_{a2}^{\text{rec}} \approx (0.13 \pm 0.03)$ cm^{-1}]. The noise in the reconstruction is mainly from the finite step size and scan region, the positional error, and the electronics. The refractive-index mismatch between the object and the background medium also contributes to the inaccuracy in the reconstructed optical properties. The fast Fourier transform (FFT) calculation takes less than 200 ms of CPU time on a SunSparc10 workstation, and the presence of multiple objects does not increase the computation complexity.

The feasibility of the FFT algorithm for imaging a scattering object was also demonstrated. The geometry is the same as in Fig. 1(a). In this case we used spherical objects as heterogeneities instead of thin slices to test the accuracy of our algorithm for imaging extended objects. Sphere 1, of radius

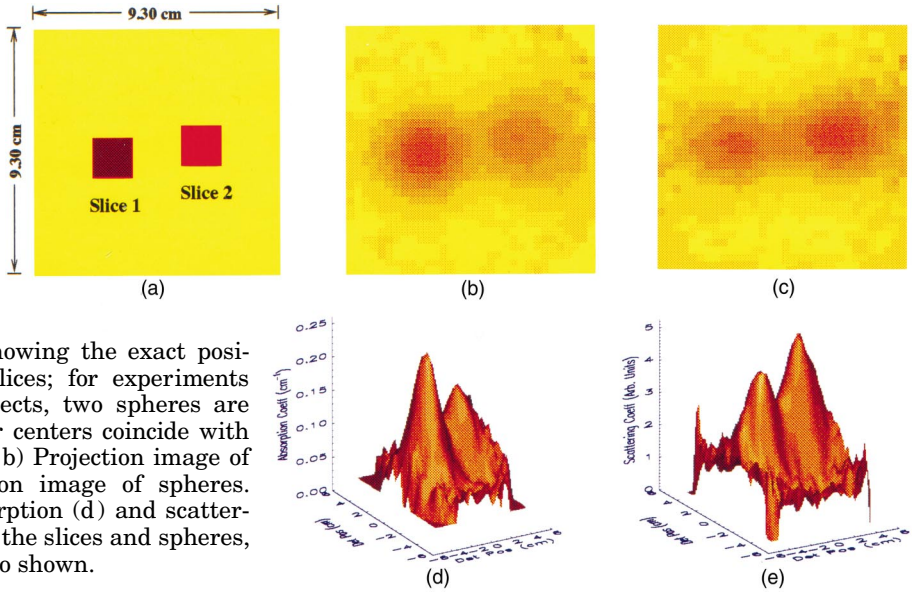

Fig. 2. (a) Slice showing the exact positions of the two slices; for experiments with scattering objects, two spheres are placed so that their centers coincide with the slice centers. (b) Projection image of slices. (c) Projection image of spheres. The recovered absorption (d) and scattering (e) properties of the slices and spheres, respectively, are also shown.

0.75 cm with $\mu_{s1}' \approx 16\ \mathrm{cm}^{-1}$, was placed at $(-1.6, -0.3, 3.0)$ cm, sphere 2, of the same radius with $\mu_{s2}' \approx 26\ \mathrm{cm}^{-1}$, was placed at $(1.6, 0.3, 3.0)$ cm. Both spheres have the same absorption coefficient as the background, i.e., $0.02\ \mathrm{cm}^{-1}$. We see from Fig. 2(c) and 2(e) that positional information about these two scattering objects is recovered. In this case we use a slice through the sphere center at $z = z_{\mathrm{obj}}$ and obtain a 2D scattering contrast image. We do not expect to reconstruct the scattering coefficients accurately since the objects are extended. However, we were still able to obtain the correct positions, and the two objects are well resolved [Figs. 2(c) and 2(e)]. Furthermore, the ratio of the reconstructed scattering coefficients is close to the true ratio, i.e., $\mu_{s2}'^{\mathrm{rec}}/\mu_{s1}'^{\mathrm{rec}} \approx 1.35$, while the true ratio is ~ 1.62.

Depth information is required for full 3D images with this diffraction tomography technique. One simple method is to use a secondary localization scheme to deduce object depth. Alternatively, two projection images of the sample along orthogonal directions provide sufficient information for 3D reconstruction.

We have successfully applied near-field diffraction tomography, diffuse-photon density waves, and FFT's to obtain projection images of hidden objects in highly scattering tissue phantoms. It may be possible to obtain clinical projection images in real time with this FFT approach. The geometry used so far has been infinite. In practice, boundary effects present important problems. On the one hand, matching materials might be used to reduce the boundary effects. On the other hand, the introduction of a surface integral term in Eq. (1) or better Green's functions (which vanish on the extrapolated boundary) may be used to incorporate boundary effects. The technique presented here provides a basis for more complicated and realistic reconstruction methods to address these issues.

We acknowledge useful discussions with Maureen O'Leary. A. G. Yodh acknowledges support from National Science Foundation grant DMR93-06814. B. Chance acknowledges support in part from the National Institute of Health grants CA 50766 and CA 60182.

References

1. A. Yodh and B. Chance, Phys. Today **48**(3), 34 (1995), and references therein.
2. See related studies in *Advances in Optical Imaging and Photon Migration*, R. Alfano, ed., Vol. 2 of Trends in Optics and Photonics Series (Optical Society of America, Washington, D.C., 1996).
3. M. Tamura, O. Hazeki, S. Nioka, and B. Chance, Ann. Rev. Physiol. **51,** 813 (1989).
4. S. R. Arridge, P. van der Zee, M. Cope, and D. T. Delpy, Proc. SPIE **1431,** 204 (1991); R. L. Barbour, H. L. Graber, Y. Wang, J. H. Chang, and R. Aronson, in *Medical Optical Tomography: Function Imaging and Monitoring*, G. Müller, ed. (SPIE Optical Engineering Press, 1993), Vol. **IS11,** p. 87; M. A. O'Leary, D. A. Boass, B. Chance, and A. G. Yodh, Opt. Lett. **20,** 426 (1995); C. P. Gonatas, M. Ishii, J. S. Leigh, and J. Schotland, Phys. Rev. E **52,** 4361 (1995); B. M. Pogue, M. S. Patterson, H. Jiang, and K. D. Paulsen, Phys. Med. Biol. **40,** 1709 (1995); H. B. Jiang, K. D. Paulsen, U. L. Osterberg, B. W. Pogue, and M. S. Patterson, Opt. Lett. **20,** 2128 (1995).
5. S. Fantini, M. A. Franceschini, G. Gaida, E. Gratton, H. Jess, W. W. Mantulin, K. T. Moesta, P. M. Schlag, and M. Kaschke, Mod. Phys. **23,** 149 (1996).
6. A. C. Kak and M. Slaney, *Principles of Computerized Tomographic Imaging* (IEEE Press, New York, 1988), Chap. 7.
7. E. Wolf, Opt. Commun. **1,** 153 (1969); E. Wolf, in *Trends in Optics*, A. Consortini, ed. (Academic, San Diego, Calif., 1996), p. 83; J. Devaney, Inverse Problems **2,** 161 (1986).
8. D. N. Pattanayak, GE Tech. Info. Series 91CRD241 General Electric; C. L. Matson, N. Clark, L. McMackin, and J. S. Fender, in *Advances in Optical Imaging and Photon Migration*, R. Alfano, ed., Vol. 2 of Trends in Optics and Photonics (Optical Society of America, Washington, D.C., 1996), p. 261.
9. M. S. Patterson, B. Chance, and B. C. Wilson, Appl. Opt. **28,** 2331 (1989).
10. A. Baños, *Dipole Radiation in the Presence of a Conducting Half-Space* (Pergamon, New York, 1996), p. 18.